Journal of Materials Chemistry C

ROYAL SOCIETY OF CHEMISTRY

PAPER

View Article Online
View Journal | View Issue

Cite this: J. Mater. Chem. C, 2020, 8, 6214

Improving the properties of 2D titanium carbide films by thermal treatment†

Hao Tang,[ab] Yina Yang,[ab] Ranran Wang*[a] and Jing Sun *[a]

Received 25th December 2019,
Accepted 23rd March 2020

DOI: 10.1039/c9tc07018d

rsc.li/materials-c

As a star of the MXene materials, 2D titanium carbide ($Ti_3C_2T_x$) has attracted broad interest from worldwide researchers in view of its potential application in energy storage, chemical sensing, electromagnetic interference shielding and flexible electronics. In order to further improve performances and satisfy the needs of emerging flexible applications, there is an urgent need to increase the electronic conductivity, environmental stability and flexibility of $Ti_3C_2T_x$ film. Herein, a two-stage thermal treatment process in an argon atmosphere at low temperature (300 °C) is proposed to address this challenge. The resulting $Ti_3C_2T_x$ film shows a 16-fold increase in electronic conductivity, while its environmental stability and flexibility are also greatly enhanced. Furthermore, systematic investigation into the microstructure and variations of $Ti_3C_2T_x$ films before and after thermal treatment shed light on the underlying mechanism, which contributes to a deeper understanding of MXene properties and offers general guidance for improving the performance of MXene films.

Introduction

MXenes, a dramatically growing family of two-dimensional transition metal carbides, nitrides and carbonitrides, have a hexagonal graphene-like structure. *Via* selective etching of the ternary MAX parent phase, MXenes are obtained with the general formula of $M_{n+1}X_nT_z$ (where M represents an early transition metal, X is C and/or N; n is 1, 2, or 3, and T_z represents the surface terminations, such as –F, –OH and –O).[1–3] Many attractive properties of MXenes have been discovered since they were obtained in 2011, including high theoretical conductivity, flexibility and hydrophilicity, which endow MXenes with great potential in many fields, such as Li-ion batteries,[4] supercapacitors,[5–7] electromagnetic interference shielding,[8,9] optoelectronics[10,11] and flexible sensors.[12,13] Although modeling can be used to discover unexpected properties of MXenes, there is a gap between these predicted effects and experimental results. For instance, Yury Gogotsi[1] predicted that Ti_3C_2 is a metallic conductor because of its small bandgap of 0.05 eV. However, the real electrical conductivity of $Ti_3C_2T_x$ film was only 2.4×10^5 S m^{-1}, which is far inferior to that of a metallic conductor.[6] The group of Zhimei Sun[14] theoretically established that 2D Ti_3C_2 can sustain a large strain of 9.5% under biaxial tension, which increased to 20% due to the addition of functional termination. By contrast, the measured value of uniaxial strain was only 1%, with the tensile strength of 22 ± 2 MPa.[6]

Defects introduced by the etching process are one factor responsible for the disparity between the realistic and theoretical properties of MXenes. And the oxidation of $Ti_3C_2T_x$ in the atmosphere will also lead to a reduction of conductivity and mechanical strength. Furthermore, MXenes are generally used in the form of assemblies, such as thin films composed of MXene nanosheets, rather than MXene monolayers. Therefore, beyond their intrinsic property, interlayer interactions and intercalants are also of great concern. How to improve the properties of MXene films has long been a question of great interest in a wide range of fields.

In order to improve the properties of MXene films, many approaches have been developed. Florian M. Römer[15] *et al.* found a controllable change of 18 ± 1% in conductivity of Ti_3C_2 film by oxygen and hydrogen plasma treatment. Before this approach is widely applied, however, it is essential to maintain the intrinsic properties of the MXene film in the atmosphere. Recently, a storage system where the water molecules and temperature were controlled has been found to achieve a constant sheet resistance of $Ti_3C_2T_x$ for 39 weeks.[16] While various methods were provided to prevent colloidal solutions of MXenes from forming due to dissolved oxygen,[17,18] researchers barely focused on an approach that could improve stability after film formation. In addition, the brittleness of $Ti_3C_2T_x$ film prevents it from many flexible and wearable applications. A previous report[6] presented composite films with excellent flexibility by mixing $Ti_3C_2T_x$ nanosheets with polymers. Although the mechanical properties of $Ti_3C_2T_x$/polymer films showed a great enhancement compared with that of both pure counterparts, the electrical conductivity dropped from 2.4×10^5 to 2.2×10^4 S m^{-1} after the addition of the insulating polymer. Therefore, a universal, simple and efficient approach that can

[a] Shanghai Institute of Ceramics, Chinese Academy of Sciences, Shanghai 200050, China. E-mail: wangranran@mail.sic.ac.cn, jingsun@mail.sic.ac.cn
[b] Center of Materials Science and Optoelectronics Engineering, University of Chinese Academy of Sciences, 19 Yuquan Road, Beijing 100049, China

† Electronic supplementary information (ESI) available. See DOI: 10.1039/c9tc07018d

concurrently improve the conductivity, environmental stability and flexibility of MXenes is urgently needed.

Hence, this study set out to assess the effect of thermal treatment on the properties of $Ti_3C_2T_x$ film. Compared with a previous study by James L. Hart,[19] this paper paid more attention to thermal treatment at low temperature (300 °C), which can improve the conductivity, environmental stability and flexibility of the $Ti_3C_2T_x$ film simultaneously. It was found that no matter which etching method was chosen, the sheet resistance of $Ti_3C_2T_x$ film after thermal treatment was smaller than that before thermal treatment by several or even a dozen times. Besides, both the environmental stability and flexibility of the $Ti_3C_2T_x$ film also exhibited a distinguished improvement. Moreover, the microstructure and terminal group variations of $Ti_3C_2T_x$ film before and after thermal treatment were characterized to clarify the mechanism of how thermal treatment affected the conductivity, environmental stability and flexibility of $Ti_3C_2T_x$ film.

Result and discussion

Synthesis of $Ti_3C_2T_x$ nanosheets

The synthesis of $Ti_3C_2T_x$ nanosheets and the following thermal treatment were conducted according to the procedure shown in Fig. 1. To remove the surface oxide layer and obtain fresh material, the ternary MAX parent phase (Ti_3AlC_2) was first reacted with hydrofluoric acid (HF) prior to intercalation. Then, tetramethylammonium hydroxide (TMAOH), an organic base, was exploited to etch Al with an amphoteric nature. And the colloidal solution was shaken violently in order to achieve the delamination of $Ti_3C_2T_x$ nanosheets, which were separated from the thick layer by centrifugation. After that, the $Ti_3C_2T_x$ nanosheets dispersed in solution were gathered onto polytetrafluoroethylene (PTFE) membrane by vacuum filtration. Finally, $Ti_3C_2T_x$ film was annealed under the protection of a stable argon flow. Different annealing temperatures were investigated and 300 °C was found to be the optimum annealing temperature, since the lowest sheet resistance was obtained, as shown in Fig. S1 (ESI†). Therefore, $Ti_3C_2T_x$ films were all annealed at the temperature of 300 °C in the following work unless otherwise stated.

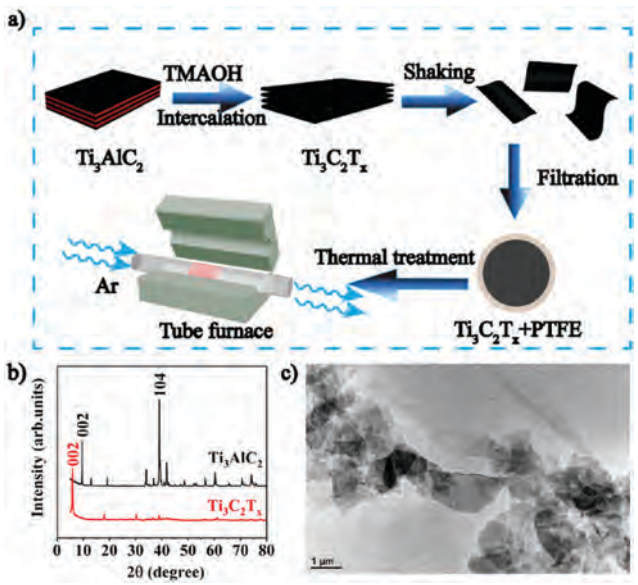

Fig. 1 (a) Schematic illustration of $Ti_3C_2T_x$ synthesis and the subsequent thermal treatment. (b) XRD patterns of Ti_3AlC_2 (MAX phase) and $Ti_3C_2T_x$. (c) TEM images of $Ti_3C_2T_x$ nanosheets.

Fig. 1(b) compares the structure of the two powders before and after intercalation using X-ray diffraction. The pattern drawn with a black line corresponds to pure-phase Ti_3AlC_2, which has a typical hexagonal symmetry ($P6_3/mmc$) formed by two layers. Another pattern is identified as the delamination of $Ti_3C_2T_x$ nanosheets according to the disappearance of the (104) peak. The change of XRD patterns demonstrates the successful removal of the Al atomic layer and the intercalation of TMA^+ ions. In addition, the position of the (002) peak shifts to a lower 2θ value in contrast to the MAX phase, implying the increase of spacing between nanosheets. As shown in Fig. 1(c), transmission electron microscopy (TEM) was utilized to clearly observe the boundaries of $Ti_3C_2T_x$ nanosheets. The image indicates that the $Ti_3C_2T_x$ nanosheets have irregular shapes and their lateral size ranges from 1 to 3 μm.

Optoelectronic properties of $Ti_3C_2T_x$ film

A series of $Ti_3C_2T_x$ films with different thickness were fabricated and annealed. The sheet resistance variation of $Ti_3C_2T_x$ films was investigated systematically, as exhibited in Fig. 2(a). Herein, the thickness of $Ti_3C_2T_x$ films was determined according to the concentration and dosage of the suspension, which was explained in detail in the Experimental section. As expected, a noteworthy decrease in the sheet resistance was observed with the increase of the film thickness, from 662 Ω sq^{-1} at the thickness of 50 nm to 24.5 Ω sq^{-1} at the thickness of 4 μm. After thermal treatment, it is apparent that the sheet resistance of the different $Ti_3C_2T_x$ films all decreased prominently, and it decreased more for thicker films. For example, the sheet resistance decreased from 24.5 to 1.5 Ω sq^{-1} after thermal treatment when the thickness of the $Ti_3C_2T_x$ film is 4 μm. Specific variations in sheet resistance (R_0/R, where R_0 and R stand for the sheet resistance before and after annealing, respectively) are displayed in the inset of Fig. 2(a). What stands out in this chart is that the sheet resistance before thermal treatment was about 16 times that after thermal treatment when the thickness was greater than or equal to 400 nm, while it only dropped several times after thermal treatment when the thickness was less than 200 nm. Besides, it was found that no matter which etching method is chosen, the sheet resistance of $Ti_3C_2T_x$ film would decrease after thermal treatment. For $Ti_3C_2T_x$ film with the thickness of 200 nm based on the glass substrate, our experimental results indicate that the sheet resistance of the sample etched by TMAOH was reduced by 3–4 times after thermal treatment, which was similar to the result obtained by utilizing the mixture of lithium fluoride (LiF) and hydrochloric acid (HCl), while that of the sample etched by HF was less obvious (about 1–2 times).

Another experiment was designed to assess the influence of TMAOH dosage on sheet resistance. As shown in Fig. 2(b),

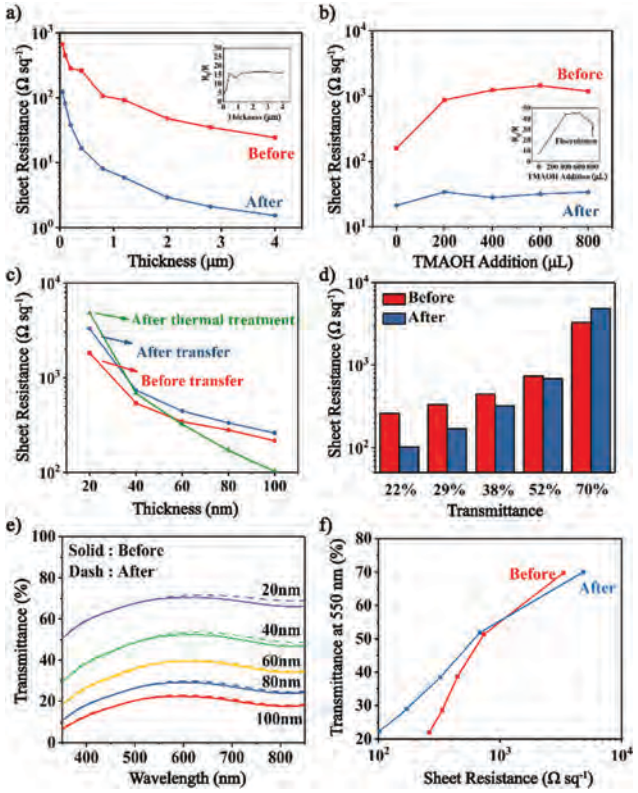

Fig. 2 (a) Sheet resistance of $Ti_3C_2T_x$ films with different thicknesses before and after thermal treatment. Inset: Specific variations of sheet resistance (R_0/R). (b) Sheet resistance of $Ti_3C_2T_x$ films (0.8 μm) upon the addition of different amounts of TMAOH before and after thermal treatment. Inset: Specific variations of sheet resistance (R_0/R). (c) Sheet resistance of $Ti_3C_2T_x$ films with different thicknesses before being transferred to the glass substrate (red), after being transferred to the glass substrate (blue), and after thermal treatment based on the glass substrate (green). (d) Sheet resistance of $Ti_3C_2T_x$ film before and after thermal treatment at different transmittance. (e) UV-vis spectra of $Ti_3C_2T_x$ films with different thicknesses before and after thermal treatment. (f) Relation between sheet resistance and transmittance of the $Ti_3C_2T_x$ film before and after thermal treatment.

the extra addition of TMAOH (200 μL per time, 25 wt%) elevated the sheet resistance of $Ti_3C_2T_x$ film by about an order of magnitude before thermal treatment. The variation of sheet resistance was related to the intercalation of TMA^+ ions, which led to a larger contact resistance between $Ti_3C_2T_x$ nanosheets. Since there was no obvious elevation in sheet resistance upon the further addition of TMAOH, it was speculated that no more TMA^+ ions can be intercalated into the interspace of $Ti_3C_2T_x$. In particular, the sheet resistance of $Ti_3C_2T_x$ film showed a decrease when TMAOH addition reached 800 μL, which was due to the flocculation of $Ti_3C_2T_x$ nanosheets. With the functionality of plenty of OH^-,[20] the charge balance was broken and $Ti_3C_2T_x$ nanosheets were bonded more tightly, corrsponding to the drop of sheet resistance. However, the sheet resistance basically remained consistent after thermal treatment no matter how much TMAOH was added. This indicated that the increase of sheet resistance caused by additional TMAOH can be completely eliminated through thermal treatment.

In order to study the transmission spectra, $Ti_3C_2T_x$ films were transferred onto transparent substrates, and during the transfer process, the conductive pathway of $Ti_3C_2T_x$ film showed slight damage. Therefore, the sheet resistance of $Ti_3C_2T_x$ film increased appreciably, as shown in Fig. 2(c). After thermal treatment, an apparent decrease in the sheet resistance was observed and the variation became less prominent with the decrease of film thickness, consistent with the tendency disclosed in Fig. 2(a). The sheet resistance of $Ti_3C_2T_x$ film even increased after thermal treatment when the thickness was 20 nm, which may be attributed to the mild oxidation of $Ti_3C_2T_x$. The variation degree of sheet resistance is clearly shown in Fig. 2(d), where different values of transmittance correspond to different film thicknesses. The transmission spectra of $Ti_3C_2T_x$ films over the visible range were recorded using a UV-vis spectrophotometer and are shown in Fig. 2(e). No significant differences were found between the transmittance spectra in the range from 350 to 850 nm before and after thermal treatment, indicating the negligible impact of thermal treatment on the optical properties of $Ti_3C_2T_x$ films.

The optoelectronic properties of $Ti_3C_2T_x$ films before and after thermal treatment are further compared in Fig. 2(f). It is obvious that the films after treatment are more conductive than those before treatment in most cases. A brief approach to distinguish the optoelectronic properties of transparent electrodes is by comparing the figure of merit (FoM), which is defined as the ratio of σ_{DC} (electronic conductivities) and σ_{opt} (optical conductivities),[21] and it can be calculated according to the formula

$$T = \left(1 + \frac{Z_0\sigma_{opt}}{2R_s\sigma_{DC}}\right)^{-2}$$

where Z_0 represents the free space impedance and the value is 377 Ω (physical constant). The transmittance and sheet resistance of $Ti_3C_2T_x$ film with the thickness of 20 nm were 70% and 3300 Ω sq^{-1}, respectively, and the FoM was calculated to be 0.29, which decreased to 0.20 after thermal treatment. Nevertheless, $Ti_3C_2T_x$ films thicker than 20 nm all gained higher values of FoM after thermal treatment, suggesting the enhancement of optoelectrical properties by thermal treatment. The most notable FoM value after thermal treatment is 1.65 (R_s = 102.4 Ω sq^{-1} and T = 22.4%), which is better than that of water-based $Ti_3C_2T_x$ films[22] and liquid-exfoliated graphene films,[21] implying the potential application of $Ti_3C_2T_x$ films as transparent electrodes.

Mechanism of sheet resistance reduction

To reveal the mechanisms of sheet resistance reduction, variations in microstructures and elements were characterized. $Ti_3C_2T_x$ film with a layered structure and a number of wrinkles on the surface was observed before thermal treatment from top-view and cross-sectional SEM images (Fig. 3(a) and (c)). After thermal treatment, a majority of wrinkles were removed and $Ti_3C_2T_x$ films became smoother and more compact (Fig. 3(b) and (d)), which may be attributed to the removal of water and TMAOH molecules from the interlayers and will lead to a notable reduction in the contact resistance among $Ti_3C_2T_x$ nanosheets. In addition, the structure of $Ti_3C_2T_x$ films before and after thermal treatment was characterized by X-ray diffraction (Fig. 3(e) and Fig. S3, ESI†). Fig. S3 (ESI†) shows

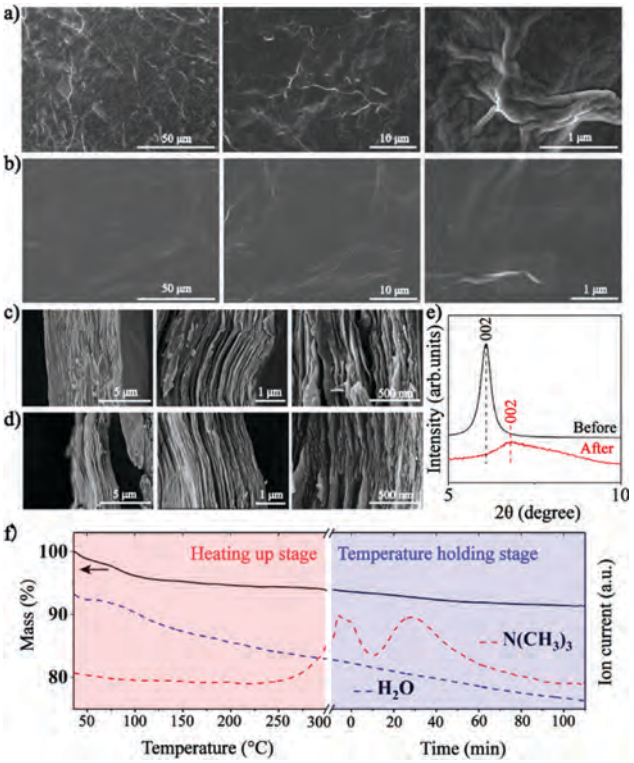

Fig. 3 (a) Top-view SEM images of $Ti_3C_2T_x$ films before and (b) after thermal treatment. (c) Cross-sectional SEM images of $Ti_3C_2T_x$ films before and (d) after thermal treatment. (e) XRD patterns of $Ti_3C_2T_x$ films before and after thermal treatment. (f) TG-MS images of $Ti_3C_2T_x$ in two-stage thermal treatment.

the XRD patterns of $Ti_3C_2T_x$ films before and after thermal treatment in a larger range (5–65°), where the characteristic peak of Ti_3AlC_2 (104) centered at 39° cannot be found, indicating that the $Ti_3C_2T_x$ film is pure. The position of the (002) diffraction peak, which relates to the reflections of crystal planes, represents the spacing between $Ti_3C_2T_x$ nanosheets. According to the Bragg equation, the (002) peak shifted from 6.1° to 6.8° after thermal treatment, indicating that the spacing decreased from 7.27 Å to 6.49 Å. The shift of the (002) peak in the XRD patterns also confirmed the densification of $Ti_3C_2T_x$ films. With the protection of argon, the residual organic matter in $Ti_3C_2T_x$ film was carbonized during thermal treatment, and the formation of amorphous carbon led to a decrease of overall crystallinity of the $Ti_3C_2T_x$ film, which was responsible for the decrease of (002) peak intensity, as shown in Fig. 3(e). This explanation was verified by the C 1s XPS spectrum (Fig. S2, ESI†). Compared with the characteristic peak (C–Ti–T_x) of $Ti_3C_2T_x$ nanosheets, the carbon impurities increased obviously after thermal treatment.

The reason for structural densification of $Ti_3C_2T_x$ film was further investigated by using thermogravimetric analysis together with mass spectrometry (TG-MS). The test conditions of thermogravimetric analysis are completely consistent with the thermal treatment process, during which $Ti_3C_2T_x$ film was heated to 300 °C at a rate of 3 °C min^{-1} and held for 2 h in an argon atmosphere. The thermal treatment included two stages, heating up and a temperature holding stage, which corresponded to the two graphs shown in Fig. 3(f), respectively. In the first stage, heating $Ti_3C_2T_x$ film to 300 °C led to a 6.18% reduction in weight, which was mainly due to the removal of interlayer water. A peak corresponding to the loss of water appeared at 100 °C in the curve, indicating the removal of absorbed water molecules. However, owing to hydrogen bonds and the capillary effect, water molecules cannot be removed completely at the temperature of 100 °C. Therefore, the desorption of water was observed during the whole heating up process whereas the signal of trimethylamine ($N(CH_3)_3$) showed no significant change until 250 °C. A subsequent temperature holding stage at 300 °C caused a 2.49% decrease in weight, which was mostly related to the decomposition of TMA^+. Two peaks contributed by $N(CH_3)_3$ were observed at this stage, testifying the decomposition of TMA^+. TMA^+ is a large organic ion that is mainly distributed on the surface and in the interlayers of $Ti_3C_2T_x$ films. The first peak related to $N(CH_3)_3$ at 250 °C originated from the decomposition of adsorbed TMA^+ on $Ti_3C_2T_x$ film. In addition, another significant signal corresponding to the decomposition product of TMA^+ arose during the temperature holding stage, indicating the removal of interlayered TMA^+ ions. Consequently, the second stage of thermal treatment is essential for the complete removal of TMA^+ ions and it is also crucial for the improvement of film properties. By contrast, a previous study[19] mostly focused on the variation of sheet resistance during continuous heating to high temperature, while the holding stage at low temperature was utterly ignored. Our work demonstrated that the temperature holding stage had an important contribution to the elimination of residual organic compounds and water molecules, so that $Ti_3C_2T_x$ films with better conductivity were obtained. Furthermore, a suitable temperature holding stage for $Ti_3C_2T_x$ film avoided the generation of a heterogeneous phase, such as TiC and TiC_xO_{1-x}, which usually existed in previous work.[23]

The variations in elements and valence states after thermal treatment were characterized by XPS. Fig. 4 provides the deconvolution of F 1s, N 1s, O 1s and Ti 2p XPS spectra before and after thermal treatment, respectively. The valence bonds of each element and the corresponding binding energies are summarized in Table S1 (ESI†). A single peak centered at 685.2 eV is observed from the F 1s XPS spectrum (Fig. 4(a)), which can be ascribed to the F–Ti valence bond. It is obvious that the peak area becomes smaller after thermal treatment, indicating a decrease of –F (Fig. 4(b)). The TMA^+ peak (centered at 402.9 eV) could only be identified before thermal treatment. Another apparent difference was found between the XPS spectral patterns of N 1s before and after thermal treatment, which showed that the cations of the intercalant (TMA^+) were completely decomposed after thermal treatment. In addition, the position of the C–N peak shifted to a higher binding energy after thermal treatment, which may be attributed to the novel carbonitrides decomposed from $[N(CH_3)_4]^+$.

Signals corresponding to the O element were fitted to three peaks, as shown in Fig. 4(c). And the three chemical bonds mostly arise from AlO_2^- and/or $Al(OH)_4^-$ terminal groups, as noted in previous studies.[24] What stands out in the O XPS spectra is the growth of all three peak areas after thermal treatment, indicating a slight increase in the content of the $Al(OH)_4^-$ group. As shown

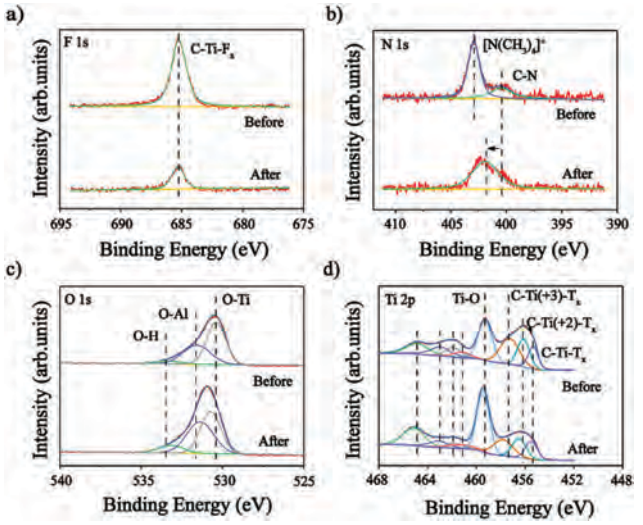

Fig. 4 Deconvolved peak of (a) F 1s, (b) N 1s, (c) O 1s and (d) Ti 2p XPS spectra of $Ti_3C_2T_x$ films before and after thermal treatment.

in Fig. S4 (ESI†), the peak of the Al 2p XPS spectrum also indicates the existence of Al–O, consistent with the results of the O 1s spectrum.

As shown in Fig. 4(d), the Ti XPS spectrum consists of four doublets with the area ratio equal to 2 : 1, which represent the feature of two types of spin–orbit (Ti $2p_{3/2}$ and Ti $2p_{1/2}$). The peak centered at 459.2 eV indicates the existence of Ti–O, most of which originates from AlO_2^- and/or $Al(OH)_4^-$ in the fresh sample. This peak area shows a remarkable expansion after thermal treatment, suggesting the increased content of AlO_2^- and/or $Al(OH)_4^-$, consistent with the analysis of O 1s XPS spectra. Besides, three peaks centered at 455.3, 456.1 and 457.2 eV represent other terminal groups connected to Ti elements, such as –F, –OH and –O. Their peak areas show a reduction after thermal treatment, which indicates a decrease in the total content of other terminal groups. The main finding from the analysis of XPS spectra is that thermal treatment at 300 °C leads to an increased content of AlO_2^- and/or $Al(OH)_4^-$ and a decreased content of other terminal groups, such as –F and TMA^+.

Stability and flexibility of $Ti_3C_2T_x$ film

The influence of thermal treatment on the stability of $Ti_3C_2T_x$ films was also investigated. Continuous resistance monitoring of $Ti_3C_2T_x$ films before and after thermal treatment was carried out to analyse their stability in the atmosphere, and the results are displayed in Fig. 5(a). The resistance variation (R/R_0) of $Ti_3C_2T_x$ film without thermal treatment increased to 15 after aging in the atmosphere for eighteen days, while it only reached 9 in the sample treated by thermal treatment, indicating the improvement in the stability of the $Ti_3C_2T_x$ film. In order to reveal the underlying mechanism, the wetting angle of $Ti_3C_2T_x$ film was measured and is shown in Fig. S5 (ESI†). It is obvious that the wetting angle of $Ti_3C_2T_x$ film increases from 60° to 67°, which represents a slight decrease in hydrophilicity after thermal treatment (Fig. S5(a) and (b), ESI†). The removal of –OH from $Ti_3C_2T_x$ nanosheets was mainly responsible for the

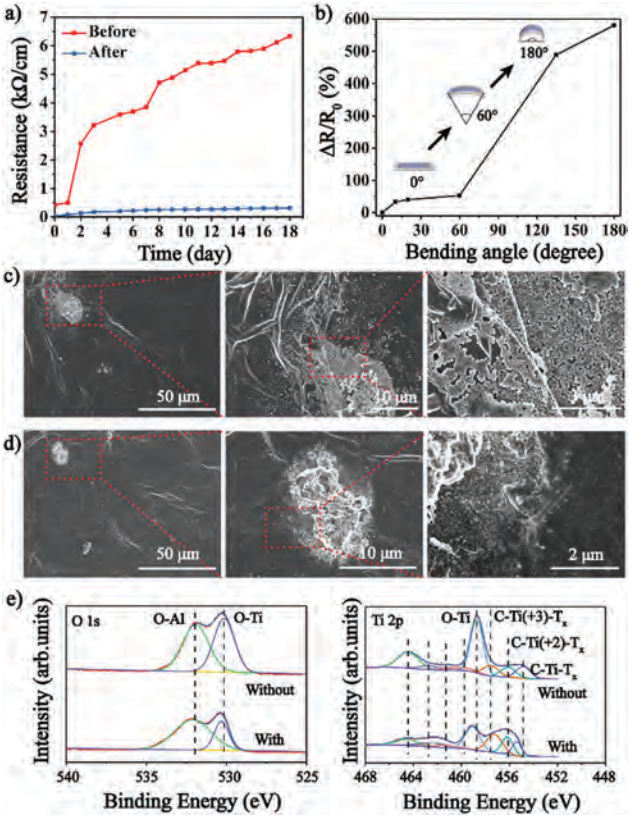

Fig. 5 (a) Continuous resistance monitoring of $Ti_3C_2T_x$ film before and after thermal treatment in the atmosphere for eighteen days. (b) Bending tests of the thermally treated $Ti_3C_2T_x$ film. (c) Top-view SEM images of $Ti_3C_2T_x$ films aged for eighteen days without thermal treatment. (d) Top-view SEM images of thermally treated $Ti_3C_2T_x$ films aged for eighteen days. (e) The deconvolved peak of the O 1s and Ti 2p XPS spectra of $Ti_3C_2T_x$ films aged for eighteen days with and without thermal treatment.

change in hydrophilicity.[10] Comparing the wetting angles shown in Fig. S5(a) and (c) (ESI†), it can be seen that the oxidation in the atmosphere made $Ti_3C_2T_x$ film more hydrophilic on account of the formation of oxidation products. For $Ti_3C_2T_x$ films aged for eighteen days, the wetting angle of the untreated sample decreased from 60° to 31°, while there was only a 5° reduction in the treated sample. This is because less –OH groups make it harder to absorb water in the atmosphere, so that $Ti_3C_2T_x$ nanosheets have less opportunity to react with dissolved oxygen in water. This explains the main reason for the improved stability of $Ti_3C_2T_x$ film after thermal treatment.

To further evaluate the oxidation extent of $Ti_3C_2T_x$ films aged in the atmosphere for eighteen days with and without thermal treatment, microstructure and terminal groups were characterized by scanning electron microscopy (SEM) and X-ray photoelectron spectroscopy (XPS), respectively. It is noteworthy that these results entirely support the above analysis of stability in the atmosphere. As shown in Fig. 5(c) and (d), numerous light-colored particles appeared in the top-view SEM images after aging, indicating the formation of oxidation products. By comparison, fewer particles were observed in the $Ti_3C_2T_x$ film with thermal treatment, again proving the enhanced stability.

In addition, the XPS spectra of $Ti_3C_2T_x$ films aged for eighteen days with and without thermal treatment are compared in Fig. 5(e). The valence bonds of Ti and O as well as the relevant binding energies are summarized in Table S2 (ESI†). The distinction between the XPS spectra of the $Ti_3C_2T_x$ film before and after aging is that most O no longer originates from AlO_2^- and/or $Al(OH)_4^-$, but from its oxidation products. The signals corresponding to O element are fitted to two peaks (O–Al and O–Ti), and the peak area of the sample with thermal treatment is smaller than that of the sample without thermal treatment, which is in accordance with the variation of the Ti–O peak in the Ti 2p XPS spectra. The results indicate that less oxidation products formed in the thermally treated $Ti_3C_2T_x$ film. In addition, three peaks centered at 454.8 456.1 and 457.6 eV, which are shown in the Ti 2p XPS spectrum of the untreated sample, are related to the terminal groups connected to $Ti_3C_2T_x$ nanosheets, and these peaks of the sample with thermal treatment are more obvious than those of the sample without thermal treatment, implying that thermal treatment contributed to the retention of more $Ti_3C_2T_x$ nanosheets after aging. Taken together, these results suggest that the sample after thermal treatment contained more $Ti_3C_2T_x$ rather than oxidation products after aging.

Another interesting finding is that the flexibility of $Ti_3C_2T_x$ film was also enhanced by thermal treatment. For $Ti_3C_2T_x$ films before thermal treatment, a slight deformation could lead to vast visible cracks, and conductive networks were completely destroyed. This brittleness prevents $Ti_3C_2T_x$ film from many flexible and wearable applications. After thermal treatment, the flexibility was greatly improved and bending tests could be employed to assess its flexibility. And the change of relative resistance after one bend at different angles is provided in Fig. 5(b). The change of relative resistance reached 50% when the bending angle is 60°. A dramatic rise in the relative resistance of $Ti_3C_2T_x$ film was observed with further enlargement of the bending angle. Finally, it reached 600% when the bending angle was 180°. Furthermore, the durability of $Ti_3C_2T_x$ film after thermal treatment is demonstrated in Fig. S6 (ESI†). The change of relative resistance gradually increased and reached 14 in the 100th bend when the bending angle was 30°. At the bending angle of 60°, the fluctuation remained stable in the initial cycles. However, it became sharp after the 65th cycle. Nevertheless, no visible cracks were found in the $Ti_3C_2T_x$ film treated thermally after the cycle bending test. A possible explanation for the improvement of flexibility is that the removal of $[N(CH_3)_4]^+$ and –OH (mentioned in Fig. 4(b)) after thermal treatment resulted in a weaker coulomb interaction between $Ti_3C_2T_x$ nanosheets, so that the sliding of nanosheets was promoted, which can dissipate the tensile stress and avoid the formation of notable cracks.

Experimental section

Synthesis of $Ti_3C_2T_x$ MXenes

$Ti_3C_2T_x$ nanosheets were obtained by selectively etching the atomic layer of aluminium from the corresponding MAX phase (Ti_3AlC_2). In order to remove the oxide layer on the surface of Ti_3AlC_2, 3 g of Ti_3AlC_2 was added to a premixed solution of HF (15 mL, 40 wt%) and deionized water (15 mL). The mixture reacted for 30 min at room temperature under stirring. And the acquired suspension was repeatedly washed with deionized water and isolated by centrifugation at 6000 rpm for 8 min until the supernatant was neutral. The fresh Ti_3AlC_2 without oxides was gathered on polypropylene membrane using vacuum filtration. The resulting powder was frozen in a refrigerator for 30 min and then freeze dried overnight. Subsequently, 300 mg of Ti_3AlC_2 was added to 3.6 mL of TMAOH, and the mixture was stirred for 24 h at room temperature. Etched $Ti_3C_2T_x$ was washed once with deionized water, and centrifuged at 10 000 rpm for 20 min. The obtained deposit was dispersed in 180 mL of deionized water and was violently shaken for 10 min in centrifuge tubes. Finally, the delaminated $Ti_3C_2T_x$ nanosheets in the supernatant were separated by centrifugation at 3500 rpm for 15 min.

Vacuum filtration and thermal treatment

Following the methods mentioned earlier, the UV-vis spectrum was employed to determine the concentration of the supernatant, and a certain amount of $Ti_3C_2T_x$ suspension was diluted with ethanol and vacuum filtered on PTFE. The reference film thickness was characterized as 400 nm through the cross-sectional SEM image, when 90 mL of suspension with the absorbance of 0.2983 was used for filtration. And the thicknesses of other $Ti_3C_2T_x$ films were obtained by comparing the dosage of $Ti_3C_2T_x$ with the reference. The homogeneous film was dried for 12 h at 30 °C in a vacuum oven. Then, the dried $Ti_3C_2T_x$ film was heated to 300 °C and held for 2 h in an argon atmosphere, while the heating rate was 3 °C min^{-1}. In order to measure the transmittance of $Ti_3C_2T_x$ film, it was vacuum filtered on a mixed cellulose ester membrane (GSWP) after dilution with deionized water. Then, the film was attached to a clean glass slide. After drying for 1 h at 60 °C, the film was subsequently wetted by 1,2-dichlorobenzene and then soaked in 200 mL of acetone for 30 min. Finally, the dried $Ti_3C_2T_x$ film adhered to a glass slide was obtained for subsequent measurements.

Resistance measurement

Sheet resistance of $Ti_3C_2T_x$ films before and after thermal treatment was measured by using a linear four-point probe configuration. Each $Ti_3C_2T_x$ film was repeatedly measured at random and the average value was obtained. In addition, silver electrodes were coated on the surface of the $Ti_3C_2T_x$ film when the environment stability was continuously monitored. The resistance between two electrodes was measured using a two-probe method involving a FLUKE-15B digital multimeter.

Flexibility measurement

$Ti_3C_2T_x$ film based on PTFE was cut into 6 mm wide strips. Then, the strips were attached onto polyethylene terephthalate (PET) substrates using silicone rubber. Two copper wires 10 mm apart were extracted from each strip using silver paste. After the silicone rubber and silver paste solidified at room temperature, the sample was ready to be used for flexibility measurement. The bending durability of the $Ti_3C_2T_x$ film after thermal treatment was noted using a high-precision electronic universal

testing machine (CMT6103, MTS Systems, China) with a tensile controller and a software system.

Characterization

The concentration of $Ti_3C_2T_x$ suspension was calibrated *via* UV-visible spectrometry (PerkinElmer Lambda 950, USA). Transmission mode of the spectrometer was employed to measure $Ti_3C_2T_x$ films based on the glass substrate. XRD patterns were collected using a high-resolution multifunction X-ray diffractometer (D8 Discover Davinci, German). The morphology of $Ti_3C_2T_x$ film was characterized using a field emission scanning electron microscope (SU8220, Hitachi, Japan). A transmission electron microscope (JEM-2100F) was employed to analyse the morphology of $Ti_3C_2T_x$ nanosheets. The surface states of $Ti_3C_2T_x$ film were characterized by using X-ray photoelectron spectroscopy (ESCALAB 250).

Conclusions

In this study, we proposed a facile method to improve the electrical and mechanical properties of $Ti_3C_2T_x$. The sheet resistance of $Ti_3C_2T_x$ film dropped by more than a dozen times through a low temperature thermal treatment, and its FoM value increased from 0.64 to 1.65. Significant enhancement in the environmental stability and flexibility of $Ti_3C_2T_x$ film was also achieved by this process. The underlying mechanism was disclosed, which can be elaborated through three main variations: first of all, a reduction in the lamellar spacing and the disappearance of surface wrinkles resulted from the removal of interlayer water and TMA^+ cationic groups; second, the variation of terminal groups, including a decrease in the content of –F and –OH, and a slight increase in the content of $Al(OH)_4^-$; and last but not least, the removal of residue organics. This work provided a low temperature avenue to improve the electronic conductivity, environmental stability and flexibility of MXene films simultaneously, which is of great benefit for the practical applications of MXenes, especially in flexible electronic areas.

Conflicts of interest

There are no conflicts to declare.

Acknowledgements

This work was supported by the National Natural Science Foundation of China (Grant No. 61871368), the Youth Innovation Promotion Association CAS, the Shanghai Science and Technology Rising Star Project (17QA1404700), and the Young Elite Scientists Sponsorship Program by CAST.

References

1 M. Naguib, M. Kurtoglu, V. Presser, J. Lu, J. Niu, M. Heon, L. Hultman, Y. Gogotsi and M. W. Barsoum, *Adv. Mater.*, 2011, **23**, 4248–4253.
2 M. Alhabeb, K. Maleski, B. Anasori, P. Lelyukh, L. Clark, S. Sin and Y. Gogotsi, *Chem. Mater.*, 2017, **29**, 7633–7644.
3 M. Naguib, V. N. Mochalin, M. W. Barsoum and Y. Gogotsi, *Adv. Mater.*, 2014, **26**, 992–1005.
4 X. Xie, M.-Q. Zhao, B. Anasori, K. Maleski, C. E. Ren, J. Li, B. W. Byles, E. Pomerantseva, G. Wang and Y. Gogotsi, *Nano Energy*, 2016, **26**, 513–523.
5 M. Ghidiu, M. R. Lukatskaya, M.-Q. Zhao, Y. Gogotsi and M. W. Barsoum, *Nature*, 2014, **516**, U78–U171.
6 Z. Ling, C. E. Ren, M.-Q. Zhao, J. Yang, J. M. Giammarco, J. Qiu, M. W. Barsoum and Y. Gogotsi, *Proc. Natl. Acad. Sci. U. S. A.*, 2014, **111**, 16676–16681.
7 C. Zhang, B. Anasori, A. Seral-Ascaso, S.-H. Park, N. McEvoy, A. Shmeliov, G. S. Duesberg, J. N. Coleman, Y. Gogotsi and V. Nicolosi, *Adv. Mater.*, 2017, **29**, 1702678.
8 F. Shahzad, M. Alhabeb, C. B. Hatter, B. Anasori, S. M. Hong, C. M. Koo and Y. Gogotsi, *Science*, 2016, **353**, 1137–1140.
9 S. Zhao, H.-B. Zhang, J.-Q. Luo, Q.-W. Wang, B. Xu, S. Hong and Z.-Z. Yu, *ACS Nano*, 2018, **12**, 11193–11202.
10 M. A. Hope, A. C. Forse, K. J. Griffith, M. R. Lukatskaya, M. Ghidiu, Y. Gogotsi and C. P. Grey, *Phys. Chem. Chem. Phys.*, 2016, **18**, 5099–5102.
11 Y. I. Jhon, J. Koo, B. Anasori, M. Seo, J. H. Lee, Y. Gogotsi and Y. M. Jhon, *Adv. Mater.*, 2017, **29**, 8.
12 Y. Yang, L. Shi, Z. Cao, R. Wang and J. Sun, *Adv. Funct. Mater.*, 2019, **29**, 1807882.
13 E. Lee, A. V. Mohammadi, B. C. Prorok, Y. S. Yoon, M. Beidaghi and D.-J. Kim, *ACS Appl. Mater. Interfaces*, 2017, **9**, 37184–37190.
14 Z. Guo, J. Zhou, C. Si and Z. Sun, *Phys. Chem. Chem. Phys.*, 2015, **17**, 15348–15354.
15 F. M. Romer, U. Wiedwald, T. Strusch, J. Halim, E. Mayerberger, M. W. Barsoum and M. Farle, *RSC Adv.*, 2017, **7**, 13097–13103.
16 Y. Chae, S. J. Kim, S. Y. Cho, J. Choi, K. Maleski, B. J. Lee, H. T. Jung, Y. Gogotsi, Y. Lee and C. W. Ahn, *Nanoscale*, 2019, **11**, 8387–8393.
17 W. F. Kuhs, C. Sippel, A. Falenty and T. C. Hansen, *Proc. Natl. Acad. Sci. U. S. A.*, 2012, **109**, 21259–21264.
18 E. Lee, A. V. Mohammadi, B. C. Prorok, Y. S. Yoon, M. Beidaghi and D. J. Kim, *ACS Appl. Mater. Interfaces*, 2017, **9**, 37184–37190.
19 J. L. Hart, K. Hantanasirisakul, A. C. Lang, B. Anasori, D. Pinto, Y. Pivak, J. T. van Omme, S. J. May, Y. Gogotsi and M. L. Taheri, *Nat. Commun.*, 2019, **10**, 10.
20 D. Zhao, M. Clites, G. Ying, S. Kota, J. Wang, V. Natu, X. Wang, E. Pomerantseva, M. Cao and M. W. Barsoum, *Chem. Commun.*, 2018, **54**, 4533–4536.
21 S. De and J. N. Coleman, *ACS Nano*, 2010, **4**, 2713–2720.
22 K. Hantanasirisakul, M. Q. Zhao, P. Urbankowski, J. Halim, B. Anasori, S. Kota, C. E. Ren, M. W. Barsoum and Y. Gogotsi, *Adv. Electron. Mater.*, 2016, **2**, 7.
23 L. Shen, X. Y. Zhou, X. L. Zhang, Y. Z. Zhang, Y. L. Liu, W. J. Wang, W. L. Si and X. C. Dong, *J. Mater. Chem. A*, 2018, **6**, 23513–23520.
24 J. Xuan, Z. Wang, Y. Chen, D. Liang, L. Cheng, X. Yang, Z. Liu, R. Ma, T. Sasaki and F. Geng, *Angew. Chem., Int. Ed.*, 2016, **55**, 14569–14574.

